Transparent microelectrode arrays integrated with microprisms for electrophysiology and simultaneous two-photon imaging across cortical layers

Qianru Yang[1,2], Bingchen Wu[1,2], Elisa Castagnola[1], May Yoon Pwint[1,2], Alberto L. Vazquez[2,3,4], X. Tracy Cui[1,2,4]

[1] Department of Bioengineering, University of Pittsburgh, United States.

[2] Center for Neural Basis of Cognition, University of Pittsburgh and Carnegie Mellon University, United States.

[3] Department of Radiology, University of Pittsburgh, United States.

[4] McGowan Institute for Regenerative Medicine, University of Pittsburgh, United States.

Abstract

Electrophysiology is a vital tool in neuroscience research and translational treatment. It records or modulates neuronal activities with high temporal but low spatial resolutions. Optical technology such as two-photon microscopy (TPM), could complement electrophysiology with large-scale imaging at cellular resolution. Combining these two could provide a powerful platform that coordinates multimodal functions. However, prior attempts have been limited to the superficial brain from a top-down optical view. Here, we describe a novel combination of transparent microelectrode arrays (MEAs) with glass microprisms for electrophysiology and simultaneous optical imaging of all cortical layers in a vertical plane. We tested our device in Thy1-GCaMP6 mice for over 4 months and demonstrated its capability for multisite single unit recording, microstimulation, and TPM calcium imaging. Using this setup, we revealed the neuronal network activity across multiple cortical layers in response to microstimulation with varying depths and parameters. This work presents a multi-modal tool that extends integrated electrophysiology and optical imaging from the superficial brain to the whole cortical column, which will greatly advance neuroscience research and neurotechnology development.

Keywords

Microprism, electrophysiology, calcium imaging, microstimulation, two-photon microscopy

1. Introduction

Understanding the complex neural network in the brain is one of the biggest challenges in neuroscience. Electrophysiology has been a crucial method since the discovery of action potential in the 19th century [1], which directly links neural functions with electricity. Microelectrode arrays (MEAs), including the Utah array and Michigan array, is the most widely used approach to record or modulate neural activities [2-9]. Studies using in vivo electrophysiology have revealed the functions of different brain regions, building the foundation for basic and translational neuroscience. However, little is known about the true spatial distribution of the neurons we are interfacing with MEA in vivo [10]. Besides, it is still challenging to identify large numbers of individual neurons from the convoluted recording data. Recent breakthroughs in optical imaging techniques, such as in vivo two-photon microscopy (TPM) [11-13], could provide important complementary information. Large-scale calcium imaging has shown dynamic activities of hundreds of neurons at the same time with cellular resolution [14-17]. In addition, developments of endogenous or exogenous fluorescent labeling for specific molecules or cell types further allow analyzing a rich number of cellular and subcellular activities [18-25]. Combining electrophysiology with optical imaging could leverage the advantages of both methods, offering an appealing solution for studying the structure and function of the brain at the same time.

There have been several attempts for simultaneous electrophysiology and optical imaging. Rigid silicon electrodes have been inserted into the brain at an angle (~30 degrees relative to the brain surface) to enable imaging of the brain-electrode interface [26-31]. Such configuration suffers from acute bleedings caused by the implanted electrode and chronic fibrous tissue growth at the brain surface, which significantly decreases the imaging depth of TPM from ~600μm (no implant) to ~ 300μm (acute implant) or ~ 150μm (chronic implant) [32, 33]. The opaque electrode also blocks the light for imaging tissue underneath. Transparent electrodes have recently drawn a lot of interest due to their compatibility with optical modalities. Typically, a transparent electrode is microfabricated by patterning conductive materials on a transparent and flexible insulating substrate (e.g., parylene C, SU-8, and polyimide). Two categories of conductive materials have been utilized in electrode fabrication, transparent conductive materials

such as indium tin oxide (ITO) and graphene, and non-transparent metal materials such as gold and platinum. Almost totally transparent ITO or graphene MEA have achieved low crosstalk electrocorticography (ECoG) recording and stimulations with concurrent TPM imaging or optogenetic modulations [34-40]. However, the inherent low conductivity of the non-metal materials limits the miniaturization of these devices for higher precision electrophysiology. On the other hand, several groups have explored the possibility of metal-based transparent MEA [41-43]. Due to the non-transparent property of metal materials, this kind of MEA seeks to minimize the metal traces while adding conductive coatings to improve its electrochemical performance. For example, Qiang et al. designed a transparent gold (Au) nano-mesh MEA with poly(3,4-ethylene dioxythiophene)-poly(styrene sulfonate) (PEDOT: PSS) coating. This metal-based transparent MEA outperformed previous graphene and ITO microelectrodes in both impedance and charge injection limit (CIL) by more than one order of magnitude, at the cost of reduced optical transparency (67%) [43]. Despite these achievements, all previous works have been optically limited to the superficial brain (layer1-3). While the laminar structure of the cortex has been illustrated a long time ago and is widely used in building computational neural networks [44-47], the dynamics of cortical microcircuits among large numbers of neurons remain poorly understood [48]. A methodology to monitor and modulate neuron populations in both superficial and deep layers simultaneously in vivo could greatly promote our understanding of how the cortical neural microcircuit works and computes.

Here we describe an approach that integrates a transparent MEA with a glass microprism, enabling electrophysiology and simultaneous optical imaging from a vertical view throughout all cortical layers. The transparent MEA achieved high-quality electrophysiology including low impedance, high charge injection limit (CIL), and stable electrophysiology by using platinum (Pt) as the conductive material combined with nano Pt coating. The transparency of the MEA is improved through a simple design—a ring shape of the electrode sites—which allows light to pass through the center. Whole cortical column imaging is realized by the microprism implantation, which changes the light path 90 degrees to present a vertical view [49-52]. Although there were concerns about tissue damage caused by implanting a 1 mm microprism, our group recently showed evidence of minimum inflammatory responses towards chronic microprism implantations by TPM imaging in living mice for 32 weeks [53]. In this work, we first attach the transparent MEA onto the microprism, and then implant the integrated device into

the animal, avoiding an extra trauma of electrode insertion. We test this MEA-on-microprism device in Thy1-GCaMP6 mice for over 4 months, showing results of intracortical single unit neural recording, microstimulation, and large-scale two-photon calcium imaging from the brain surface to cortical layer 5/6. Through simultaneous microstimulation and TPM imaging, we acquired the first suite of calcium images from neuron populations across multiple cortical layers in response to microstimulation with a series of parameters, providing new insights for choosing microstimulation parameters in neuroscience research and neural prosthetics applications.

2. Results

To enable the integration of MEAs and microprism, we custom-designed and fabricated the transparent MEAs using standard photolithography techniques (see details in the Materials and Methods section and Fig. 1a-e). The 16-channel MEA uses SU-8 as the insulating substrate and Pt as the conductive material. SU-8 has been extensively utilized in biomedical devices due to its high transparency, low young's modulus, and high yield strength [54-56]. Pt is a common material for stimulation electrodes for its chemical inertness [57-59]. The insulating SU-8 layers are optimized to be 9 µm thick on each side, balancing between flexibility and robustness. To allow optical imaging through the MEA, the width of the metal connections is minimized to 2 µm within the 1 x 1 mm^2 tip region that is attached to the imaging face of the microprism, and the electrode sites adopt a ring-shaped design to let light pass through the center (Fig. 1f). The ring-shaped site has an external diameter of 50 µm and an internal diameter of 40 µm, to match the geometric area (706 μm^2) with a standard 30 µm-diameter round electrode. The 16 channels are arranged in a 4x4 configuration with an inter-electrode spacing of 200 µm (center-to-center)

(figure 1f).

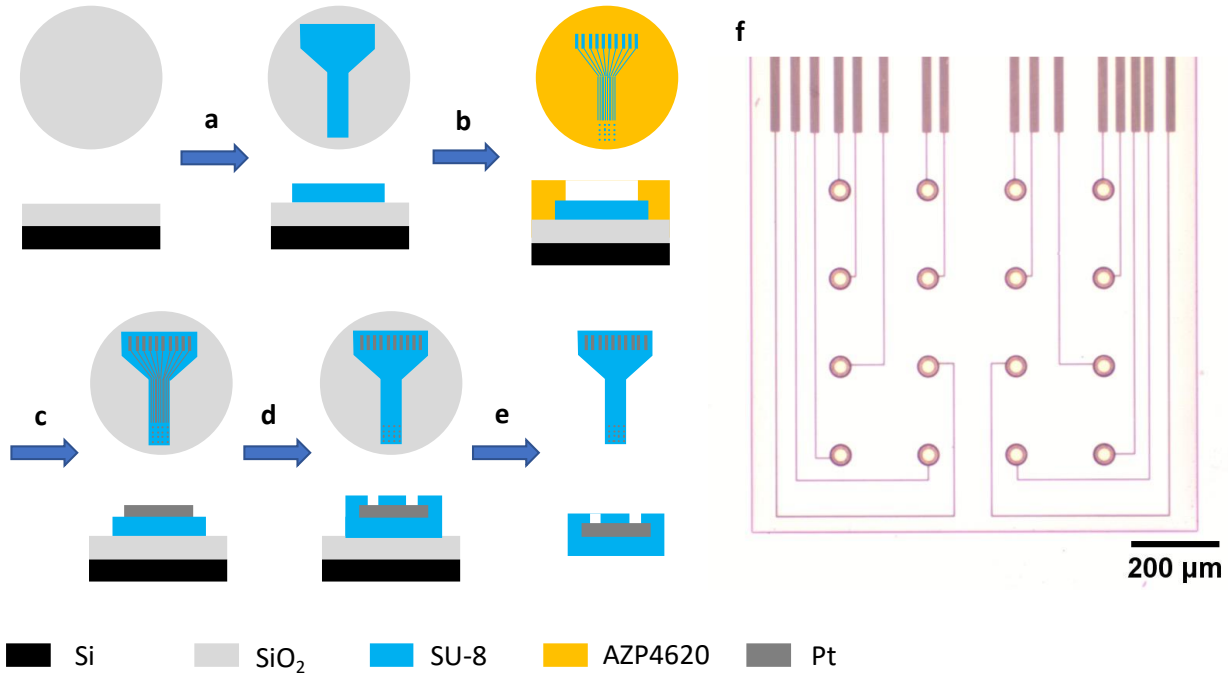

Figure 1. Fabrication of the flexible and transparent MEA.
(a)~(e) Schematic of photolithography procedures. The top and side views of each step are shown in stacks (dimensions not to scale). (a) SU-8 is spin coated, exposed, and then developed as the bottom insulation on a silicon (Si) wafer with 1µm of silicon dioxide (SiO_2) on the top. (b) AZ4620 positive photoresist is spin-coated, exposed, and developed as the mask for the metal layer. (c) 100nm Platinum (Pt) is evaporated on the wafer with a 10nm Ti adhesion layer and lifted off in acetone to form the conductive metal part. (d) Another layer of SU-8 is spin coated, exposed, and developed as the top insulation. (e) The wafer is placed in buffered oxide etchant to release the MEA device. (f) Optical microscopy image of the face ("tip") region of the MEA showing the 4x4 ring-shaped array and the thin connecting traces.

We electrochemically deposited nano-Pt coatings on the MEA to improve its electrochemical properties (Fig. 2a). The magnified SEM of the nano-Pt coating shows a cauliflower-like nanostructured morphology, while the surface of a bare Pt electrode is relatively flat. These images clearly show that the nano-Pt coating drastically increases the effective electrochemical area of the electrode. Consistent with the SEM results, we observed a significant increase in the charge storage capacity (CSC) of the electrode from 1.06±0.15 mC cm^{-2} to

6.05±0.17 mC cm^{-2}, as calculated from the time integral of the last cyclic voltammogram (CV) cycle before and after the nano-Pt coating (Fig. 2b). We also observed that the nano-Pt coating decreased the impedance of the electrode in the low-frequency range (Fig. 2c). Specifically, the impedance at 1kHz dropped from 75.32±23.70 kΩ to 41.34±2.96 kΩ. After nano-Pt deposition, the CIL of the electrode is estimated to be 2.27mC cm^{-2}, as we can deliver 80 µA cathodic current for 200 µs before the E_{mc} reaches -0.6V versus Ag/AgCl (Fig. 2d). Compared with other state-of-art transparent electrode arrays, our nano-Pt coated ring electrodes show superb impedance, slightly better than the Au/PEDOT:PSS nanomesh microelectrodes and 30x to 100x better than graphene or ITO electrodes scaled to the same size [35, 36, 40, 43].

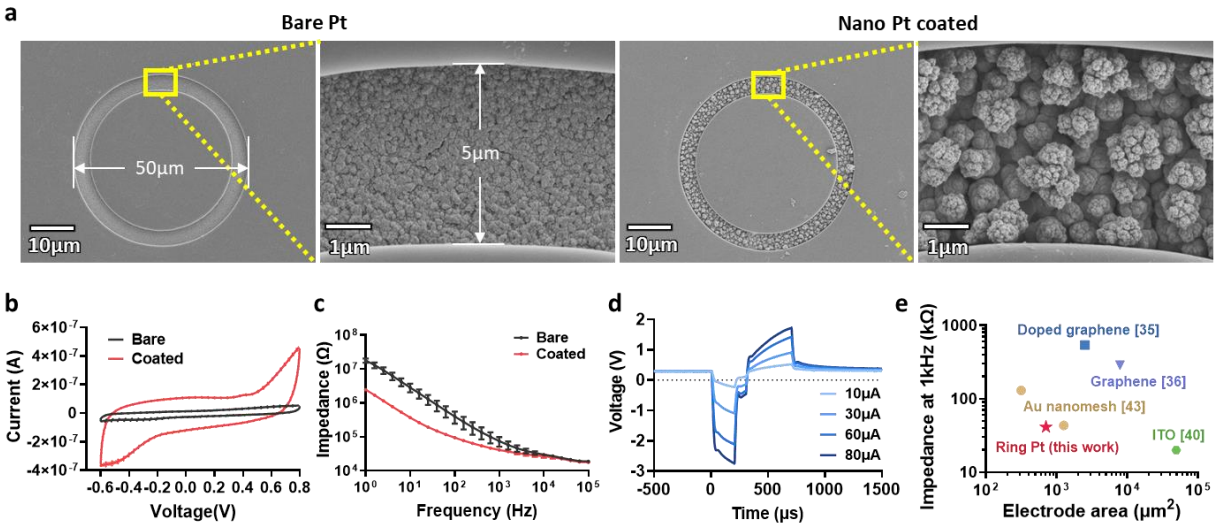

Figure 2. In vitro characterizations of MEA before and after nano-Pt deposition.

(a) Representative SEM images of bare Pt and nano-Pt coated electrode sites. Magnified views on the right side in each condition show the nanostructured surface morphologies. (b) CV of a representative MEA before and after nano-Pt coating. N=16 electrode sites. Data are presented as mean ± SD. (c) Electrochemical impedance spectroscopy (EIS) of an MEA before and after nano Pt coating. N=16 electrode sites. Data are presented as mean ± SD. (d) Voltage transients in response to bi-phasic, asymmetric (I_c= 2 * I_a) current pulses. The cathodic current amplitudes were ramped up from 10 µA to 80 µA. (e) The impedance at 1kHz and electrode area of our MEAs compared with other state-of-art transparent MEAs.

The procedure to assemble a functional microprism/MEA device is illustrated in Fig. 3. We designed and purchased the 16-channel PCB that connects the Omnetics connector with 16 metal pads and two metal rings for the ground/reference electrode. The MEA was bonded to the PCB with an anisotropic conductive film (ACF) cable. We tested the CV and EIS of the MEA to ensure proper connections and electrochemically deposited nano-Pt onto the Pt electrode sites. Meanwhile, the microprism was attached to three pieces of coverglass by UV curable transparent optical glue. Then we adhered the tip of MEA to the microprism and the cover glasses also with optical glue. Finally, we soldered a silver wire to the ground and reference pads on the PCB and applied a thin layer of silicone onto the traces and wires to strengthen the insulation and the mechanical durability of the device. Before the implantation surgery, we ran electrochemical characterizations of the fully assembled device and sterilized it with ethylene oxide (EtO) sterilization.

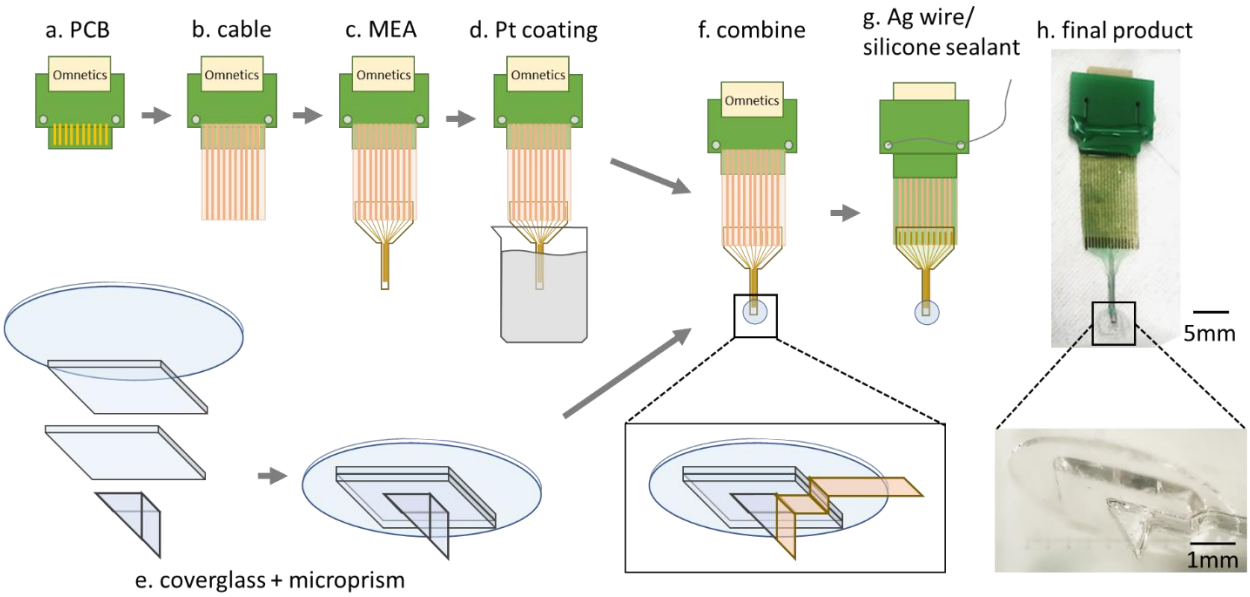

Figure 3. Assembly procedure of the functional MEA-on-microprism device.

(a) Customized PCB with standard 16-channel Omnetics connector. (b) Connect the heat-seal ACF cable to the metal traces on PCB. (c) Bond our previously fabricated MEA to the ACF cable. (d) Electrochemically deposit nano-Pt onto MEA by applying a constant voltage. (e) Glue microprism and three pieces of cover glasses together using UV-cured transparent glue. (f)

Adhere the tip of MEA to the microprism's imaging face using transparent glue. (g) Solder a silver wire to the PCB as the ground/reference. Spread a thin layer of silicone sealant onto the backside of the cable, the trace region on MEA, and cover all the exposed bare metal parts. (h) Photo of a finished assembly. The inset reveals the magnified view of the MEA tip on the microprism. Scale bar=5mm for the top photo, and 1mm for the inset.

To test the capability of our device in vivo, we implanted the MEA-on-microprism in the visual cortex of mice for over 4 months. The surgical procedure is similar to implanting just the microprism as described in previous publications [49, 50, 53]. A metal head frame was attached to the skull for head-fix experiments later. We created a 4mm x 4mm square cranial window between sutures in GCaMP6s mice, generally over the sensory and visual cortex of the animal. The orientation of the microprism was pre-designed to target the visual cortex when implanted. After removing dura matter, we made a 1mm long and 1mm deep incision and slide the microprism/MEA vertically with a vacuum line bond to a stereotaxic arm. Another stereotaxic arm that holds the PCB was approaching the brain at an angle (~30 degrees) at a synchronized pace with the vacuum arm. After inserting the device fully into the brain, we sealed the cranial window with silicon and dental cement on the edges. The MEA was grounded to a stainless-steel bone screw on the skull on the contralateral side. Extra ACF cable was folded under PCB and the device outside of the brain was fixed to the skull with dental cement embedding (Fig. 4a).

Successful surgery can maintain a clear and stable cranial window for a long time (Fig. 4b). Through the implanted microprism, we were able to monitor neuronal activities from the brain surface down to layer 5/6, confirmed by the void in the expression of layer 4 neurons in Thy1-GCaMP6s animals (Fig. 4c). Aligned with previous work [53], the imaging distance is around 500 µm from the microprism vertical face after several weeks of recovery. The ring shape design of the MEA minimizes the width of the metal to the scale of micro blood vessels, allowing light to pass through the center so that the tissue behind the electrodes can be imaged. In TPM images, the shadow of the thin metal connection is almost invisible beyond 50 µm from the microprism and the shadow of electrode sites becomes invisible around 200 µm away from the microprism

(Fig. 4c).

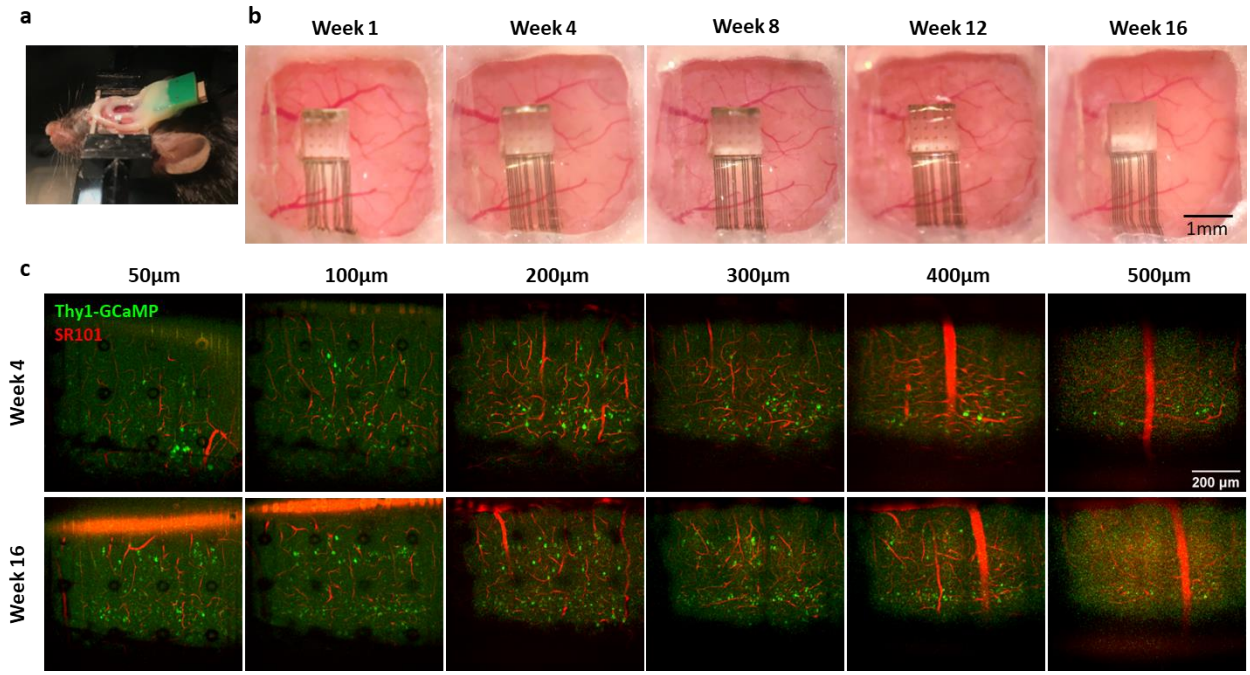

Figure 4. The MEA-on-microprism device implanted in mice allows high quality optical imaging over 16 weeks.

(a) Bird's eye view of the cranial window and the device on a head-fixed mouse. (b) Images of the cranial window under a surgical microscope for over 16 weeks. (c) TPM imaging of spontaneous neural activities (green) and blood vessels (red) through the MEA-on-microprism device. Neural calcium activity image is max projected from a 3 min time-lapse scan. Left to right: increasing distances from the microprism.

We characterized the electrochemical properties of the MEAs implanted in three animals using a two-electrode setup, where a stainless-steel bone screw on the contralateral brain hemisphere served as the counter electrode. Note that for in vitro electrochemical measurements we used a three-electrodes setup, thus the results are not directly comparable. We analyzed 22 electrode sites from three animals that maintained a reasonable 1kHz impedance (<1 MΩ) at most of the time. The CSC of individual electrode sites fluctuates over time as shown in Fig. 5a. The average CSC also possesses ups and downs over time—it increased in the first week then dropped back and reached the lowest value at week 2, followed by a slightly increasing trend

afterward (Fig. 5a). The CSC at week12 and week 16 were significantly higher than day 0 (immediately after the implantation surgery) (Fig. 5a). The mean impedance at 1kHz of the MEAs increased in the first 2 weeks, then declined from week 2 to week 8, and increased back from week 8 to week 16 (Fig. 5b). The impedance at week 2, week 6, and week 8 were significantly different from day 0 (Fig. 5b). The shape of the CV curve and the impedance spectrum change from a representative electrode site are plotted over time in Figures 5c and 5d. In the first 2 weeks, the CV graph of this representative site shrunk by about half. While at weeks 4 and 8, the CV almost returned to its original shape. Later at weeks 12 and 16 post-surgery, the CV curves broadened evidently (Fig. 5c). The impedance of this electrode site increased a little from day 0 to week 2 (Fig. 5d), which may indicate the formation of glial scars. After week 4, the impedance decreased in all frequencies and remained low compared to day 0 (Fig. 5d). In accordance, the voltage transients induced by the same 5uA pulse curves, the E_{mc}, decreased from around -1 V (week 2) to -0.6 V (week 4~ week 16) (Fig. 5e). The widened CV curve after week 12 and the impedance drop across frequencies indicate that the effective electrochemical surface area of the electrode has increased [60]. This phenomenon could be explained by insulation cracking or liquid penetrating under the insulation layer [61, 62]. Despite this, the changes of CSC and impedance at 1kHz for most sites stayed within the same magnitude throughout 16 weeks, showing the long-term stability of our custom-fabricated MEA.

The implanted MEA was able to record single-unit activities on resting awake animals for over 16 weeks (Fig. 5f). Spike waveforms are sorted using the automatic k-means feature in Offline Sorter software. Noise clusters were manually excluded.

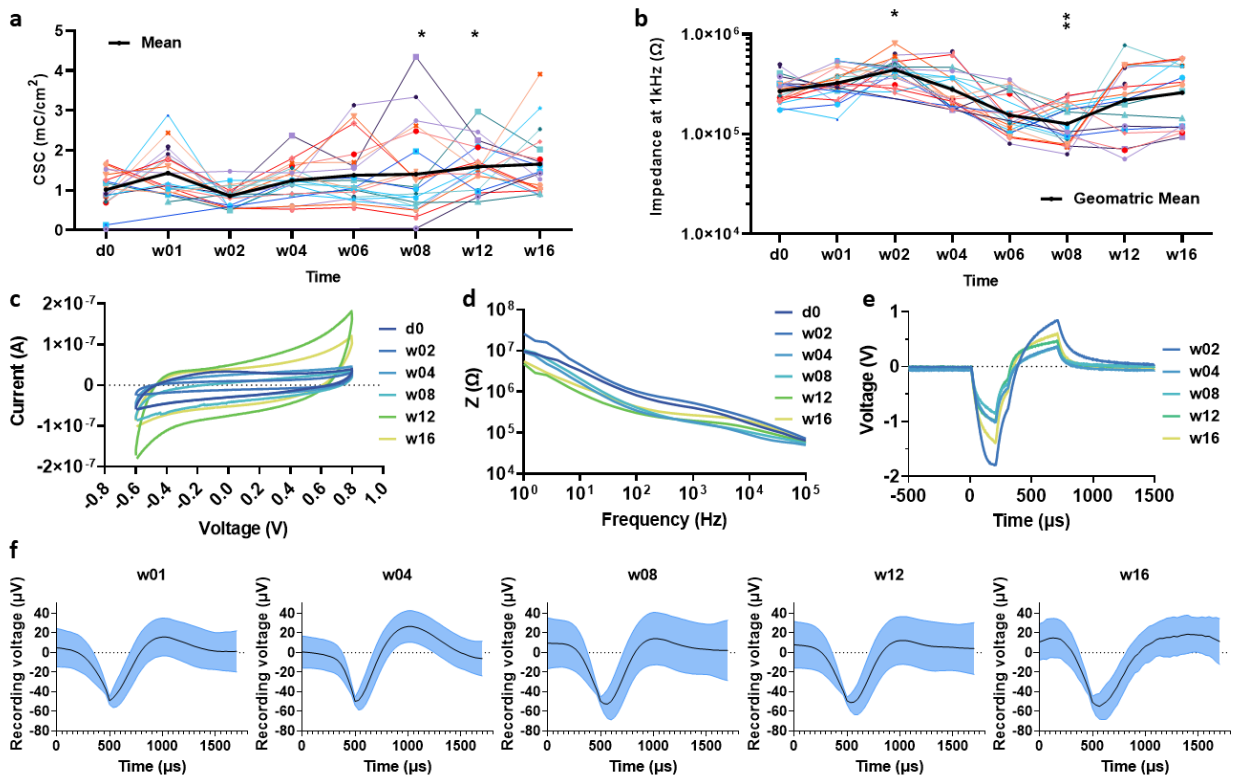

Figure 5. In vivo electrochemical characterizations and electrophysiological recordings over 16 weeks.

(a) Charge storage capacity of the MEA over time (n=22 sites from 3 animals). Individual sites are plotted in assorted colors, and the mean value is presented in a thick black line. (b) The impedance at 1kHz over time (n=22 sites from 3 animals). Individual sites are plotted in assorted colors, and the mean value is presented in a thick black line. In (a) & (b), we ran a one-way ANOVA followed by Dunn's multiple comparisons to test for differences against time point d0. * $p<0.05$, ** $p<0.01$. (c) Representative CV curve of one electrode site over time. Different colors indicate different time points. (d) Representative impedance spectrum of one electrode site over time. Different colors indicate different time points as in (c). (e) Representative voltage transients in response to the same current pulse (bi-phasic, asymmetric, 5μA cathodic leading) over time. Different colors indicate different time points. (f) Representative waveforms extracted from spontaneous recordings in an awake mouse over time. Spikes are sorted using Offline Sorter software. Data are presented as mean ± SD.

Next, we examined the TPM imaging of neuronal activity evoked by visual stimulation. A blue LED light was placed about 5 cm away from the contralateral eye of the mouse. After a 30-sec delay, the LED light flickers for 1 sec at 10Hz every 15 sec. By averaging 10 trials, we identified the neurons that were repetitively activated by the light stimuli (Fig. 6a). The relative fluorescent intensity change ($\Delta F/F$) of three representative neurons during the whole session is shown in Fig. 6b. The background fluorescent intensity (F) is the mean value of the first 30 sec before light stimulation. These curves corroborate that these neurons are responding to the light stimulations. After aligning the curves to the time stamp of light stimuli from the 10 trials, we learn the average response of each neuron (Fig. 6c). Neuron #1 and neuron #2 peak at the light-on period, while neuron #3 shows the largest response after light-off (Fig. 6c). These are typical responses of neurons that are sensitive to a light spot being turned on or off in the visual system [63-65]. These results indicate that the visual input circuits are preserved near the microprism/MEA face, showing the potential for studying all kinds of sensory evoked neuronal responses with this device. Simultaneous TPM imaging and recording from the MEA have been explored, but the huge photo-electric artifact deteriorates electrophysiology signals so much that we can hardly extract any meaningful information from the recording during laser scan. To achieve TPM and recording at the same time, future works could consider replacing the Pt with low photo-electric effect materials.

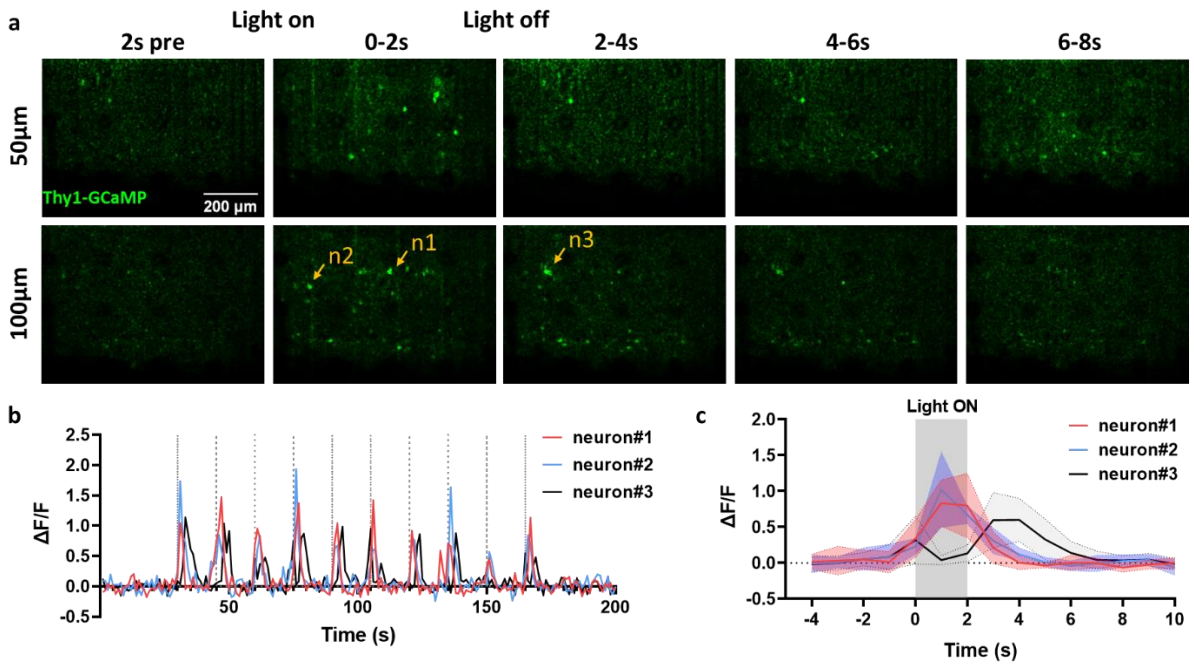

Figure 6. TPM imaging of visual stimulation (light pulses) evoked neuronal calcium responses. (a) GCaMP fluorescence changes before/during/after light stimulation. Averaged from 10 consecutive trials. n1~n3 mark the three neurons analyzed in (b) and (c). (b) GCaMP fluorescence change of three representative neurons during the whole 200s imaging session. Dotted lines indicate the onset time of each light stimulation period (1 sec). (c) Averaged fluorescence change of the three neurons relative to the light stimuli. The line with shadow represents mean ± SD.

We also conducted TPM imaging of neuronal responses to electrical stimulation delivered through the MEA on the microprism. Electrical stimulation consisted of charge-balanced square wave pulses with 200 µs cathodic phase, 100 µs interval, and 400 µs anodic phase (Fig. 7a), mimicking the parameters used in human studies [5]. The reported amplitudes here all refer to the cathodic current amplitudes. We first asked how the current amplitude of stimulation influences neuronal activation. We stimulated every available site with an impedance of < 1MOhm at 1kHz three times with a 25% duty cycle (1s ON, 3s OFF) at 50Hz and monitored the neuronal calcium activity 50µm away from the MEA surface using TPM in awake mice. The images were averaged from three stimulation periods. Near the activation threshold current (5µA), a couple of sparsely distributed neurons were activated (Fig. 7b). As we increased the

current amplitude to 10µA, more neurons near the stimulated electrode became activated (Fig. 7b). When the current amplitude reached 15µA, we observed a lot of neuropil activation around the stimulated site and that the neural response appeared to saturate at >15µA (Fig. 7b). Similar neuronal calcium responses to changing amplitudes were observed on all working electrode sites over different days. The sparse and distributed neuronal activation at 5µA is consistent with a previous TPM study [66], while here we have a vertical observation plane across all cortical layers instead of focusing on a single horizontal plane in layer 2/3. We chose 10µA for the rest of the stimulation experiments as it was just sufficient to reliably generate an obvious neural calcium response for most sites. Note that the Thy1-GCaMP6 expression is lower in layer 4 than in other cortical layers [67], we use the fluorescent dark band at around 400µm deep as a reference marker for cortical layer 4 (Fig. 7b, c).

Next, we investigated how the stimulation location affects the cortical neural network activity in response to electrical stimuli. Current pulse trains (1s, 10µA) were delivered at 50Hz from the MEA while imaging neuronal calcium responses under TPM (Supplementary Video 1). We observed that electrical stimulations from the same column of the MEA activated a similar group of neurons but with different strengths (Fig. 7c, Ch1~Ch4). Additionally, electrical stimulations at another column recruited a different cohort of neurons (Fig. 7c, Ch5~Ch6), indicating a columnar neural activation field. To qualitatively compare the strength and the distribution of the neural calcium activation, we further plotted the profile of fluorescent intensity change along the X and Y axis (Fig. 7d, e). The layer 4 (Ch2) electrode was found to elicit the strongest GCaMP response, layer 5 (Ch3) electrode the second, layer 2/3 (Ch1) and layer 6 (Ch4) electrodes lower. These results indicate that electrical stimulation may be most efficient at activating neuronal populations in general if delivered at layer 4, followed by layer 5, and less efficient at layer 2/3 and layer 6 in this stimulation paradigm. After we normalized the fluorescent intensity to the peak intensity value for each site in Fig. 8e, we noticed higher relative peaks at around 500µm deep for Ch2 and Ch6 compared to their layer2/3 neighbor electrodes Ch1 and Ch5 (Fig. 7f). These observations indicate that apart from the overall stimulation power, layer 4 electrode sites recruit relatively more deep layer (L5) neurons compared to layer 2/3 electrode sites. The impedance spectrums of these electrode sites were similar but not completely overlapping (Supplementary Figure 1), confirming that these electrode sites were not shorted and

that the difference in neural activation was unlikely to result from the variability of individual electrode sites.

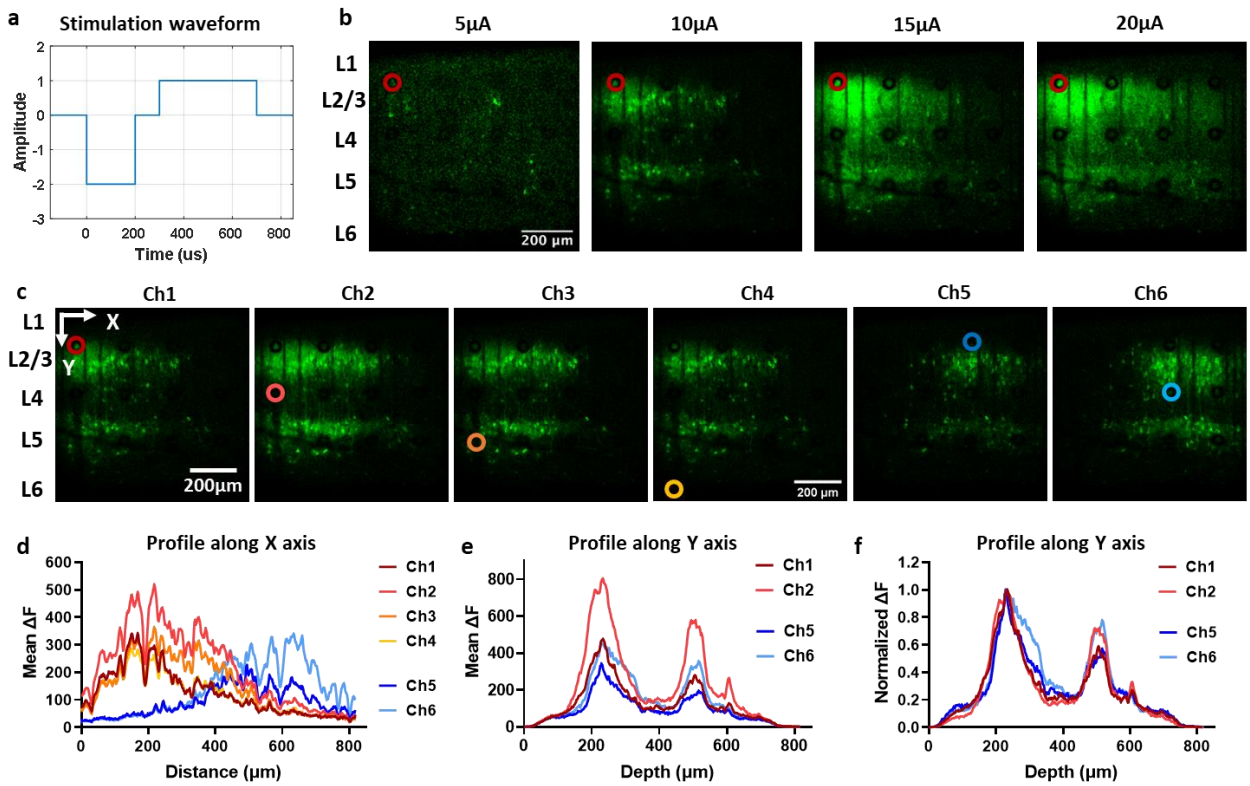

Figure 7. TPM imaging of neuronal responses to electrical stimulation reveals amplitude and location dependence.

(a) The electrical stimulation waveform used. (b) Representative TPM images of neuronal calcium activity change in response to electrical stimulation at increasing current amplitudes. The images are averaged over three repetitions of stimulation for each amplitude. The red circle indicates the location of the stimulated channel. (c) Representative TPM images of neuronal calcium activity change in response to electrical stimulation at different locations. The images are averaged over three repetitions for each electrode site. The circles in gradient colors indicate the location of the stimulated channel. (d) The fluorescent intensity profile of images in (c) is projected along the x-axis. (e) The fluorescent intensity profile of images in (d) is projected along the y-axis. (f) Normalized fluorescent intensity profile along the y-axis.

In addition to the current amplitude and electrode location, frequency is also a crucial factor that can modulate the neural response to electrical stimulation. Changing the stimulation frequency has been shown to alter the type of tactile sensation and the perception intensity in the somatosensory cortex [5, 68, 69]. There is also behavioral evidence indicating that frequency modulation of intracortical stimuli is layer-specific [70]. However, the mechanism of frequency modulation on the neural network level remains to be elucidated. With this in mind, we stimulated all the available channels of the MEA at various frequencies, ranging from 5Hz to 150Hz, while keeping the same amplitude (10 µA). Again, using in vivo TPM imaging through our device, we found that increasing the frequency of stimulation affects the neuronal activation pattern in a complex manner. Taking a layer 4 electrode site as an example: at 5Hz, the neural activation was sparse and distributed; as we increased the frequency to 50Hz, the neuronal response was much stronger, but still distributed; when we further increased the frequency, the intensity decreased, and the field of neuronal activation shrunk (Fig. 8a and b). Interestingly, although the overall neuronal activation decreased from 50Hz to 150Hz, more neurons at around 400 µm deep were activated at higher frequencies (Figures 8a and c). Moreover, the frequency modulation curve may be also depth dependent. Within the same column of electrodes on the MEA, the middle layer electrode sites (Ch2 and Ch3) induced the strongest overall neuronal response at ~50Hz, while electrodes at the superficial layer (Ch1) or the deep layer (Ch4) induced larger neuronal responses at 20Hz compared to other frequencies tested (Fig. 8d).

These stimulation experiments concerning depth dependence have been replicated in the same animal over different days. Although three of four animals survived at least 16 weeks of implantation (75% survival rate), two of them were excluded from the stimulation analysis due to poor imaging clarity or a liquid gap between the MEA and the brain tissue. Future studies may seek strategies to improve the biocompatibility of MEA materials and further investigate the depth dependence of intracortical microstimulation with a greater number of animals, finer step size in depth, and fluorescent labeling of other molecules of interest.

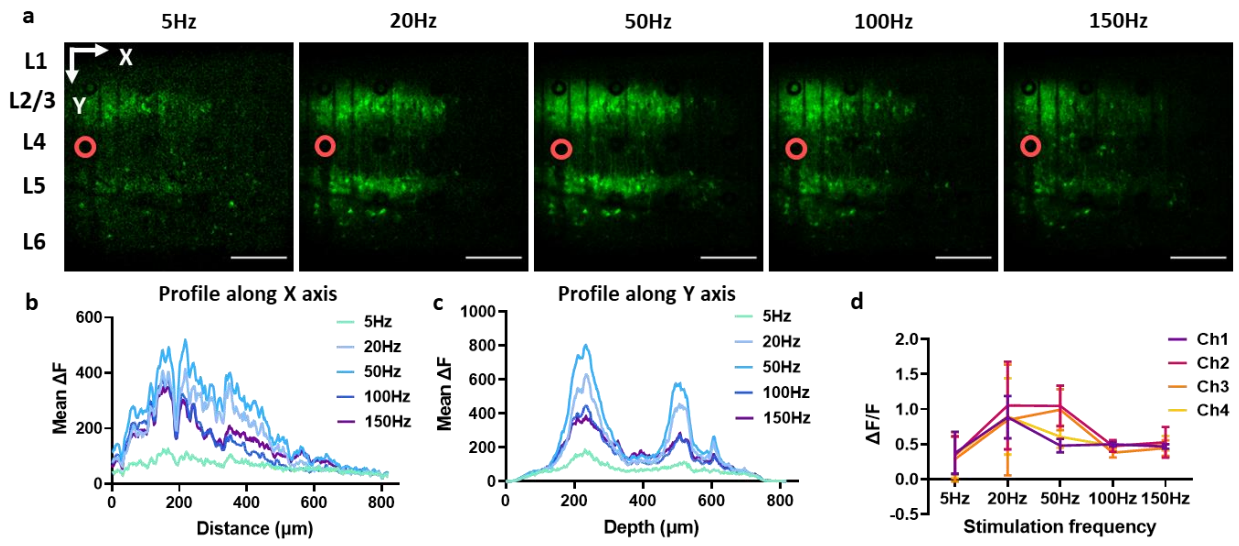

Figure 8. TPM imaging of neuronal responses to electrical stimulation reveals frequency dependence and depth dependence.

(a) Representative TPM images of neuronal calcium activity in response to electrical stimulation from an L4 site at increasing frequencies. The stimulations are bi-phasic, asymmetric square wave pulses at 10µA (cathodic) for 1 sec. The images are averaged from three repetitions of stimulation. The red circle indicates the location of the stimulated channel. This imaging plane is focused at 50µm from the MEA. Scale bar=200µm. (b) The fluorescent intensity profile of images in (a) is projected to the x-axis. (c) The fluorescent intensity profile of images in (a) is projected to the y-axis. (d) Frequency dependence curves of electrodes at different depths (Ch1~4). N=6 stimulations on two separate days.

3. Conclusions

In this work, we developed a platform that combined a transparent MEA with a microprism to enable simultaneous electrophysiology and optical imaging in a vertical plane spanning from the brain surface to the cortical layer 5/6. The custom-fabricated MEA achieves high flexibility and transparency by photolithographically patterning platinum on a flexible and transparent SU-8 substrate, plus ring-shaped electrode sites and thin traces that minimize the shadow of metal in the region of imaging. This novel MEA-on-microprism design remarkably expands the vertical depth of chronic two-photon imaging of electrode arrays from ~150 µm to

~1000 µm, visualizing multiple cortical layers simultaneously. With this setup, we were able to perform chronic TPM imaging and electrical recording/stimulation in Thy1-GCaMP6s mice for over 4 months. High-resolution TPM images of neuronal calcium activities near the MEA have been captured at the resting state and upon sensory stimuli of the animal. We observed stable in vivo electrochemical properties of the MEA and demonstrated its capability of single unit recording throughout 16 weeks of implantation. Furthermore, using this device, we demonstrated how electrode depth, stimulation amplitude, and stimulation frequency influence the neuronal calcium responses to intracortical microstimulation. To the best of our knowledge, this is the first in vivo TPM imaging work that directly visualizes the cortical multi-layer neuronal network in response to microstimulation. Our work provides simple but powerful designs for concurrent electrophysiology and optical imaging throughout all cortical layers, which could revolutionize the way of studying large-scale cortical cellular mechanisms in neuroscience research and neural prosthetic developments.

4. Methods

4.1. Fabrication of MEA

Microelectrode arrays (MEA) fabrication: Si wafer with a 1µm thick SiO2 layer (University Wafer Inc) was first cleaned by sonicating in acetone, isopropanol, and DI water sequentially for 5 mins each step. The wafer was then dried on a hot plate at 150°C for 3 mins and cleaned by O_2 plasma using a reactive ion etcher (RIE, Trion Phantom III LT) for 120s at 200 mTorr pressure and 150Watts power. The cleaned wafer was spin-coated with SU-8 2015 (MicroChemicals) at 5000rpm for 1min and soft baked at 65°C for 3 mins and 95°C for 5 mins. Then the wafer was exposed using a maskless aligner (MLA, MLA100 Heidelberg Instruments) with a dose of 400 mJ/cm2. After exposure, the SU-8 first layer was post-baked at 65°C for 3 mins and 95°C for 5 mins, developed using SU-8 developer (MicroChemicals) for 1min and cleaned by isopropanol and DI water, and hard baked at 200°C, 180°C, and 150°C for 5mins each and allowed to cool down below 95°C. The wafer was then treated with O_2 plasma with RIE for 75s at a pressure of 200 mTorr and 150W power. The cleaned wafer was then spin-coated with AZ P4620 photoresist (MicroChemicals) at 5300rpm for 1min and baked at 105°C for 5mins. After baking the wafer is exposed using MLA with a dose of 700mJ/cm2, then developed

using AZ400k 1:4 developer (MicroChemicals), cleaned by water rinsed, and dried by N2 gas flow. A mild 60s RIE O2 plasma cleaning at pressure 600 mTorr and 60W power was performed before metal deposition. 10nm Ti adhesion layer and 100nm Pt layer were evaporated on the wafer using Electron Beam Evaporator (Plassys MEB550S). Then the metal was lifted-off in acetone overnight. The next day, the wafer was cleaned by O2 plasma for 60s at 600 mTorr and 60W, then spin-coated with SU-8 2015 at 5000rpm for 1min and soft baked at 65°C for 2 mins and 95°C for 5 mins. The wafer is exposed using MLA with a dose of 400mJ/cm2, post-backed, and developed with an SU-8 developer. The wafer was then cleaned with isopropanol and water, and hard baked at 200°C, 180°C, and 150°C for 5mins each and allowed to cool down below 95°C. The MEAs were lifted off from the wafer using buffered oxide etchant (1:7) in an acid hood for 8 hours.

4.2. Electrodeposition of Pt

Nano-platinum was electrochemically formed starting from a solution containing 25mM $H_2(PtCl_6)$ in 1mM HCl, by applying a constant voltage at -0.3V for 200s. Electrochemical depositions were carried out using a potentiostat/galvanostat (Autolab, Metrohm, USA), connected to a three-electrode electrochemical cell with a platinum counter electrode and an Ag/AgCl reference electrode.

4.3. Assembly of microprism and MEA

Similar to previous work, microprism was purchased (#MPCH-1.0, Tower Optical Corporation) and adhered to three layers of cover glasses (two 3x3mm square, one 5mm round, #1 thickness, 0.15 ± 0.02 mm, Warner Instruments LLC) using a transparent glue (NOA 71, Norland Optical).

The printed circuit board (PCB) was manufactured following a customized design. The MEA was connected to the PCB using a silver heat-seal connector (P/N HST-9805-210, Elform). Specifically, the connector cable was trimmed to fit the width of PCB and MEA with a length of 1~2cm. The cable was then aligned and bonded to the PCB and MEA using a hair straightener heated to 380°F for ~30s with pressure. Two pieces of PDMS (~1mm thick) were used to pad between the heating pad and the PCB/MEA on both sides. After electrochemically depositing nano platinum onto the sites, we applied a drop of NOA 71 glue to the back side of the MEA tip

and carefully adhered the MEA to the microprism imaging face and the cover glasses, with an angled tip tweezer holding the MEA bent at ~90 degrees at the corner. Excess glue that ran to the front side of MEA was gently removed with a fine tip tweezer. The ground and reference site on the PCB was connected to a silver wire, which will be wired around the bone screw on the animal later. Finally, all the exposed traces and fragile parts were covered with a thin layer of silicone to provide additional insulation and mechanical support. Fully assembled devices were characterized with electrochemical methods described below and sterilized with the ethylene oxide sterilization process before surgery.

4.4. Electrochemical characterizations

Electrochemical impedance spectroscopy (EIS) and cyclic voltammetry (CV) measurements were used to investigate the electrode/solution interface in vitro, before implantation, and in vivo.

During the EIS measurements, a sine wave (10 mV RMS amplitude) was superimposed onto the open circuit potential while varying the frequency from 1 to 10^5 Hz. During the CV tests, the working electrode potential was swept between 0.8V and −0.6 V with a scan rate of 1V/s. Both EIS and CV measurements were carried out using a potentiostat/galvanostat (Autolab, Metrohm, USA).

In vitro, EIS and CV were performed in 1x phosphate buffered saline (PBS, composition: 11.9 mM Na_2HPO_4 and KH_2PO_4, 137 mM NaCl, 2.7 mM KCl, pH 7.4) using a three-electrode electrochemical cell configuration with a platinum counter electrode and an Ag/AgCl reference electrode.

In the brain, EIS and CV were measured using a two-electrode electrochemical cell configuration, where a stainless-steel bone screw, anchored on the contralateral skull, served as the counter and reference electrode.

4.5. Animals and surgery

Transgenic mice expressing the neuronal activity reporter GCaMP6s in cortical pyramidal neurons (male, n=3, strain Tg (Thy1-GCaMP6s) GP4.3Dkim) were used in this study and obtained from the Jackson Laboratories (Bar Harbor, ME USA). During surgery, mice were

anesthetized using ketamine (75mg/kg)/xylazine(10mg/kg) and maintained with updates of ketamine (22.5mg/kg) alone as needed. Animal fur on top of the head was trimmed off and the skin surface was then sterilized with 70% isopropyl alcohol and betadine. The animal head was fixed onto a stereotaxic frame (Narishige International USA) and the temperature was kept at 37 °C with an electric heating pad. After skin resection and skull drying with Vetbond (3M, St. Paul, MN), a rectangular stainless-steel frame (#CF-10, Narishige International USA) was adhered to the skull with dental cement (A-M Systems, Sequim, WA). We waited until the dental cement completely solidified before transferring the animal to a frame-holding stereotaxic (Narishige International USA). A stainless-steel bone screw (0.86mm shaft diameter, Fine Science Tools, Inc.) was secured on the left parietal bone of the skull as reference and ground for the electrode. Using a high-speed dental drill, we created a 4x4 mm craniotomy above the somatosensory and visual cortex over the right hemisphere. The dura mater within the cranial window was removed with a fine tip tweezer and a bent 30-gauge needle. A lance-shaped 0.1 mm thick razor blade (#72000, Electron Microscopy Sciences) was attached to a stereotaxic arm and inserted vertically then moved laterally to create a 1x1 mm incision. We applied saline and Gelfoam to the surface of the brain and waited for the bleeding to stop. The PCB of the device was anchored to a stereotaxic arm angled at about 30 degrees and was approaching the cranial window from the back of the animal. Another stereotaxic arm was oriented vertically to hold the cover glass of the microprism/MEA with a vacuum line. The microprism/MEA was inserted vertically into the incision, with the imaging surface of the microprism facing the posterior (visual cortex) of the animal. The microprism/MEA device was lowered until the round coverglass touched the skull so that the square cover glasses were contacting the brain surface with a little pressure to prevent dura and meningeal regrowth. Tiny drops of silicone sealant (Kwik-sil, World Precision Instruments) were applied around the coverglass and on the uncovered brain surface if any to seal the cranial window. The vacuum was released after dental cement secured the implant in place. The ground/reference wire was connected to the bone screw. The excessive cable was folded to the back of the PCB and covered with dental cement. After surgery, the animal was treated with 5 mg/kg ketoprofen (100 mg/ ml, Zoetis Inc., Kalamazoo, MI) and 10mg/kg Baytril solution (Henry Schein Inc.) for three days. All experimental protocols were approved by the University of Pittsburgh, Division of Laboratory Animal Resources and Institutional Animal Care and Use Committee (ARO ID: IS00018691) in

accordance with the standards for humane animal care as set by the Animal Welfare Act and the National Institutes of Health Guide for the Care and Use of Laboratory Animals.

4.6. In vivo two-photon imaging and image processing

The animal was head-fixed, free-running on a custom treadmill during two-photon imaging. The two-photon imaging system has been described in our previous publications [27, 53]. It consists of an ultra-fast laser (Insight DS+; Spectra-Physics, Menlo Park, CA), a scan head (Bruker, Madison, WI), non-descanned photomultiplier tubes (Hamamatsu Photonics KK, Hamamatsu, Shizuoka, Japan), and a 16X 0.8 NA water immersion objective lens (Nikon Instruments, Melville, NY). The excitation laser was set at a wavelength of 920 nm. Sulforhodamine 101 (SR101) (~0.05 cc; 1 mg/ml) was injected before imaging for visualization of blood vessels. For imaging neuronal calcium activities, time-series images were collected at 512 x 512 x 1 pixel and at ~1 frame per second (fps).

The time-series images were processed and analyzed using ImageJ and customized IJ1 macro scripts. The images were first denoised with a median filter and the “Despeckle” function. A background image was acquired by averaging the whole image stack or the images before any stimulation. Then we subtract the background image from every image in the time series. The resulting fluorescence change images were maximum intensity projected to a single image to capture all active neurons during the period of interest. The vasculature in Fig. 4 is the average image of the red (SR101) channel, which is superimposed on the above neural activity image in the green (Thy1-GCaMP) channel.

For quantification of neuronal calcium intensity change in Figure 7, we manually circled the neurons from the raw image stack and exported the intensity change over time. The fluorescent intensity change ratio ($\Delta F/F$) is then calculated, where F is the mean value of fluorescence intensity in the first 30s before light stimulation, and ΔF is the difference between F and the fluorescent at each time stamp. In Fig. 8 and Fig. 9, the fluorescent intensity profile along the x and y axis is measured with the “Plot profile” function in ImageJ. The image was rotated 90 degrees to change the direction of the profile projection.

4.7. Electrophysiological recording

The electrophysiological recording was performed on awake animals. Data was collected by Ripple Grapevine (Nano2+stim Ripple LLC, Salt Lake City, Utah) and Trellis software at a 30kHz sample rate. Spike waveforms were sorted in Plexon offline sorter (version 3) using the spike trains data. We first applied K-means automatic sorting algorithm to the raw data in all the channels. Then we checked the waveforms of each unit and discarded the incorrect units.

4.8. Electrical stimulation

Current-controlled stimulations were delivered using Autolab (Metrohm, USA). 1-sec long pulse trains contain biphasic, charge-balanced asymmetric square waves with various amplitudes and frequencies. Each pulse has a 200 µs cathodic phase, a 100 µs interval, and a 400 µs anodic phase. The anodic current amplitude is set at half of the cathodic current. During one imaging session, each electrode site is stimulated three times in a row; each time there is a 1-sec stimulation period and a 3-sec off period.

5. Acknowledgement

The authors thank Dr. Hui Fang and Dr. Qiang Yi for advice and materials on the heat-seal connector. This work is supported by NIH R01NS089688 and BRAIN R01NS110564.

6. Table of Contents

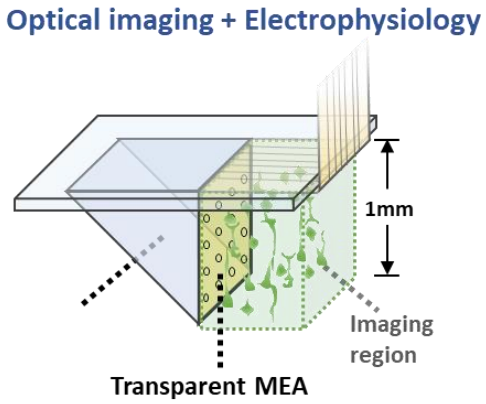

This MEA-on-microprism design integrates a 16-channel transparent electrode array with microprism to allow simultaneous electrophysiology and optical imaging throughout all cortical

layers. By implanting this device in the visual cortex of mice, we achieved single-unit recording, microstimulation, and two-photon imaging of the whole cortical column for over 4 months. Concurrent microstimulation and two-photon imaging revealed depth dependency of various stimulation parameters.

References

[1] S.M. Schuetze, The discovery of the action potential, Trends in Neurosciences 6 (1983) 164-168.
[2] H. Asanuma, S. Stoney Jr, C. Abzug, Relationship between afferent input and motor outflow in cat motorsensory cortex, Journal of Neurophysiology 31(5) (1968) 670-681.
[3] W.G. Penfield, Ferrier lecture-some observations on the cerebral cortex of man, Proceedings of the Royal Society of London. Series B-Biological Sciences 134(876) (1947) 329-347.
[4] E. Bizzi, Discharge of frontal eye field neurons during saccadic and following eye movements in unanesthetized monkeys, Experimental Brain Research 6(1) (1968) 69-80.
[5] S.N. Flesher, J.L. Collinger, S.T. Foldes, J.M. Weiss, J.E. Downey, E.C. Tyler-Kabara, S.J. Bensmaia, A.B. Schwartz, M.L. Boninger, R.A. Gaunt, Intracortical microstimulation of human somatosensory cortex, Science translational medicine 8(361) (2016) 361ra141-361ra141.
[6] G.A. Tabot, J.F. Dammann, J.A. Berg, F.V. Tenore, J.L. Boback, R.J. Vogelstein, S.J. Bensmaia, Restoring the sense of touch with a prosthetic hand through a brain interface, Proceedings of the National Academy of Sciences 110(45) (2013) 18279-18284.
[7] W.H. Dobelle, Artificial vision for the blind by connecting a television camera to the visual cortex, ASAIO journal 46(1) (2000) 3-9.
[8] J.L. Collinger, B. Wodlinger, J.E. Downey, W. Wang, E.C. Tyler-Kabara, D.J. Weber, A.J. McMorland, M. Velliste, M.L. Boninger, A.B. Schwartz, High-performance neuroprosthetic control by an individual with tetraplegia, The Lancet 381(9866) (2013) 557-564.
[9] D.M. Taylor, S.I.H. Tillery, A.B. Schwartz, Direct cortical control of 3D neuroprosthetic devices, Science 296(5574) (2002) 1829-1832.
[10] G. Buzsáki, Large-scale recording of neuronal ensembles, Nature neuroscience 7(5) (2004) 446-451.
[11] W. Denk, J.H. Strickler, W.W. Webb, Two-photon laser scanning fluorescence microscopy, Science 248(4951) (1990) 73-76.
[12] K. Svoboda, W. Denk, D. Kleinfeld, D.W. Tank, In vivo dendritic calcium dynamics in neocortical pyramidal neurons, Nature 385(6612) (1997) 161-165.
[13] C. Stosiek, O. Garaschuk, K. Holthoff, A. Konnerth, In vivo two-photon calcium imaging of neuronal networks, Proceedings of the National Academy of Sciences 100(12) (2003) 7319-7324.
[14] A. Song, A.S. Charles, S.A. Koay, J.L. Gauthier, S.Y. Thiberge, J.W. Pillow, D.W. Tank, Volumetric two-photon imaging of neurons using stereoscopy (vTwINS), Nature methods 14(4) (2017) 420-426.
[15] M.B. Bouchard, V. Voleti, C.S. Mendes, C. Lacefield, W.B. Grueber, R.S. Mann, R.M. Bruno, E.M. Hillman, Swept confocally-aligned planar excitation (SCAPE) microscopy for high-speed volumetric imaging of behaving organisms, Nature photonics 9(2) (2015) 113-119.
[16] W. Zong, H.A. Obenhaus, E.R. Skytøen, H. Eneqvist, N.L. de Jong, R. Vale, M.R. Jorge, M.-B. Moser, E.I. Moser, Large-scale two-photon calcium imaging in freely moving mice, Cell 185(7) (2022) 1240-1256. e30.
[17] L. Ghanbari, R.E. Carter, M.L. Rynes, J. Dominguez, G. Chen, A. Naik, J. Hu, M.A.K. Sagar, L. Haltom, N. Mossazghi, Cortex-wide neural interfacing via transparent polymer skulls, Nature communications 10(1) (2019) 1-13.
[18] A.A. Oliva, M. Jiang, T. Lam, K.L. Smith, J.W. Swann, Novel hippocampal interneuronal subtypes identified using transgenic mice that express green fluorescent protein in GABAergic interneurons, Journal of Neuroscience 20(9) (2000) 3354-3368.

[19] Y. Wang, T. Kakizaki, H. Sakagami, K. Saito, S. Ebihara, M. Kato, M. Hirabayashi, Y. Saito, N. Furuya, Y. Yanagawa, Fluorescent labeling of both GABAergic and glycinergic neurons in vesicular GABA transporter (VGAT)–Venus transgenic mouse, Neuroscience 164(3) (2009) 1031-1043.
[20] N.C. Flytzanis, C.N. Bedbrook, H. Chiu, M.K. Engqvist, C. Xiao, K.Y. Chan, P.W. Sternberg, F.H. Arnold, V. Gradinaru, Archaerhodopsin variants with enhanced voltage-sensitive fluorescence in mammalian and Caenorhabditis elegans neurons, Nature communications 5(1) (2014) 1-9.
[21] A. Nimmerjahn, F. Helmchen, In vivo labeling of cortical astrocytes with sulforhodamine 101 (SR101), Cold Spring Harbor Protocols 2012(3) (2012) pdb. prot068155.
[22] I. Ferezou, S. Bolea, C.C. Petersen, Visualizing the cortical representation of whisker touch: voltage-sensitive dye imaging in freely moving mice, Neuron 50(4) (2006) 617-629.
[23] H. Wang, M. Jing, Y. Li, Lighting up the brain: genetically encoded fluorescent sensors for imaging neurotransmitters and neuromodulators, Current Opinion in Neurobiology 50 (2018) 171-178.
[24] G. Miesenböck, D.A. De Angelis, J.E. Rothman, Visualizing secretion and synaptic transmission with pH-sensitive green fluorescent proteins, Nature 394(6689) (1998) 192-195.
[25] S. Okumoto, L.L. Looger, K.D. Micheva, R.J. Reimer, S.J. Smith, W.B. Frommer, Detection of glutamate release from neurons by genetically encoded surface-displayed FRET nanosensors, Proceedings of the National Academy of Sciences 102(24) (2005) 8740-8745.
[26] J.R. Eles, A.L. Vazquez, T.D. Kozai, X.T. Cui, In vivo imaging of neuronal calcium during electrode implantation: spatial and temporal mapping of damage and recovery, Biomaterials 174 (2018) 79-94.
[27] T.D.Y. Kozai, A.L. Vazquez, C.L. Weaver, S.-G. Kim, X.T. Cui, In vivo two-photon microscopy reveals immediate microglial reaction to implantation of microelectrode through extension of processes, Journal of neural engineering 9(6) (2012) 066001.
[28] X.S. Zheng, Q. Yang, A. Vazquez, X.T. Cui, Imaging the efficiency of PEDOT/CNT and iridium oxide electrode coatings for microstimulation.
[29] K.C. Stieger, J.R. Eles, K.A. Ludwig, T.D. Kozai, In vivo microstimulation with cathodic and anodic asymmetric waveforms modulates spatiotemporal calcium dynamics in cortical neuropil and pyramidal neurons of male mice, Journal of neuroscience research 98(10) (2020) 2072-2095.
[30] N.J. Michelson, J.R. Eles, A.L. Vazquez, K.A. Ludwig, T.D. Kozai, Calcium activation of cortical neurons by continuous electrical stimulation: Frequency dependence, temporal fidelity, and activation density, Journal of neuroscience research 97(5) (2019) 620-638.
[31] J.R. Eles, T.D. Kozai, In vivo imaging of calcium and glutamate responses to intracortical microstimulation reveals distinct temporal responses of the neuropil and somatic compartments in layer II/III neurons, Biomaterials 234 (2020) 119767.
[32] T.D. Kozai, J.R. Eles, A.L. Vazquez, X.T. Cui, Two-photon imaging of chronically implanted neural electrodes: Sealing methods and new insights, Journal of neuroscience methods 258 (2016) 46-55.
[33] J. Eles, A. Vazquez, T. Kozai, X. Cui, Meningeal inflammatory response and fibrous tissue remodeling around intracortical implants: an in vivo two-photon imaging study, Biomaterials 195 (2019) 111-123.
[34] P. Ledochowitsch, A. Yazdan-Shahmorad, K. Bouchard, C. Diaz-Botia, T. Hanson, J.-W. He, B. Seybold, E. Olivero, E. Phillips, T. Blanche, Strategies for optical control and simultaneous electrical readout of extended cortical circuits, Journal of neuroscience methods 256 (2015) 220-231.
[35] D. Kuzum, H. Takano, E. Shim, J.C. Reed, H. Juul, A.G. Richardson, J. De Vries, H. Bink, M.A. Dichter, T.H. Lucas, Transparent and flexible low noise graphene electrodes for simultaneous electrophysiology and neuroimaging, Nature communications 5(1) (2014) 1-10.
[36] D.-W. Park, J.P. Ness, S.K. Brodnick, C. Esquibel, J. Novello, F. Atry, D.-H. Baek, H. Kim, J. Bong, K.I. Swanson, Electrical neural stimulation and simultaneous in vivo monitoring with transparent graphene electrode arrays implanted in GCaMP6f mice, ACS nano 12(1) (2018) 148-157.

[37] M. Thunemann, Y. Lu, X. Liu, K. Kılıç, M. Desjardins, M. Vandenberghe, S. Sadegh, P.A. Saisan, Q. Cheng, K.L. Weldy, Deep 2-photon imaging and artifact-free optogenetics through transparent graphene microelectrode arrays, Nature communications 9(1) (2018) 1-12.
[38] D.-W. Park, A.A. Schendel, S. Mikael, S.K. Brodnick, T.J. Richner, J.P. Ness, M.R. Hayat, F. Atry, S.T. Frye, R. Pashaie, Graphene-based carbon-layered electrode array technology for neural imaging and optogenetic applications, Nature communications 5(1) (2014) 1-11.
[39] K.Y. Kwon, B. Sirowatka, A. Weber, W. Li, Opto-μECoG array: A hybrid neural interface with transparent μECoG electrode array and integrated LEDs for optogenetics, IEEE transactions on biomedical circuits and systems 7(5) (2013) 593-600.
[40] N. Kunori, I. Takashima, A transparent epidural electrode array for use in conjunction with optical imaging, Journal of neuroscience methods 251 (2015) 130-137.
[41] C.F. Guo, T. Sun, Q. Liu, Z. Suo, Z. Ren, Highly stretchable and transparent nanomesh electrodes made by grain boundary lithography, Nature communications 5(1) (2014) 1-8.
[42] W. Lee, D. Kim, N. Matsuhisa, M. Nagase, M. Sekino, G.G. Malliaras, T. Yokota, T. Someya, Transparent, conformable, active multielectrode array using organic electrochemical transistors, Proceedings of the National Academy of Sciences 114(40) (2017) 10554-10559.
[43] Y. Qiang, P. Artoni, K.J. Seo, S. Culaclii, V. Hogan, X. Zhao, Y. Zhong, X. Han, P.-M. Wang, Y.-K. Lo, Transparent arrays of bilayer-nanomesh microelectrodes for simultaneous electrophysiology and two-photon imaging in the brain, Science advances 4(9) (2018) eaat0626.
[44] C.D. Gilbert, Microcircuitry of the visual cortex, Annual review of neuroscience (1983).
[45] R.J. Douglas, K. Martin, A functional microcircuit for cat visual cortex, The Journal of physiology 440(1) (1991) 735-769.
[46] Y. Amir, M. Harel, R. Malach, Cortical hierarchy reflected in the organization of intrinsic connections in macaque monkey visual cortex, Journal of Comparative Neurology 334(1) (1993) 19-46.
[47] T. Binzegger, R.J. Douglas, K.A. Martin, A quantitative map of the circuit of cat primary visual cortex, Journal of Neuroscience 24(39) (2004) 8441-8453.
[48] J.M. Blackwell, M.N. Geffen, Progress and challenges for understanding the function of cortical microcircuits in auditory processing, Nature communications 8(1) (2017) 1-9.
[49] T.H. Chia, M.J. Levene, Microprisms for in vivo multilayer cortical imaging, Journal of neurophysiology 102(2) (2009) 1310-1314.
[50] M.L. Andermann, N.B. Gilfoy, G.J. Goldey, R.N. Sachdev, M. Wölfel, D.A. McCormick, R.C. Reid, M.J. Levene, Chronic cellular imaging of entire cortical columns in awake mice using microprisms, Neuron 80(4) (2013) 900-913.
[51] R.J. Low, Y. Gu, D.W. Tank, Cellular resolution optical access to brain regions in fissures: imaging medial prefrontal cortex and grid cells in entorhinal cortex, Proceedings of the National Academy of Sciences 111(52) (2014) 18739-18744.
[52] L. Beckmann, X. Zhang, N.A. Nadkarni, Z. Cai, A. Batra, D.P. Sullivan, W.A. Muller, C. Sun, R. Kuranov, H.F. Zhang, Longitudinal deep-brain imaging in mouse using visible-light optical coherence tomography through chronic microprism cranial window, Biomedical optics express 10(10) (2019) 5235-5250.
[53] Q. Yang, A.L. Vazquez, X.T. Cui, Long-term in vivo two-photon imaging of the neuroinflammatory response to intracortical implants and micro-vessel disruptions in awake mice, Biomaterials 276 (2021) 121060.
[54] M. Hopcroft, T. Kramer, G. Kim, K. Takashima, Y. Higo, D. Moore, J. Brugger, Micromechanical testing of SU‐8 cantilevers, Fatigue & Fracture of Engineering Materials & Structures 28(8) (2005) 735-742.
[55] S.-H. Huang, S.-P. Lin, J.-J.J. Chen, In vitro and in vivo characterization of SU-8 flexible neuroprobe: From mechanical properties to electrophysiological recording, Sensors and Actuators A: Physical 216 (2014) 257-265.

[56] Z. Chen, J.-B. Lee, Biocompatibility of su-8 and its biomedical device applications, Micromachines 12(7) (2021) 794.
[57] G.S. Brindley, W.S. Lewin, The sensations produced by electrical stimulation of the visual cortex, The Journal of physiology 196(2) (1968) 479-493.
[58] S.B. Brummer, M. Turner, Electrochemical considerations for safe electrical stimulation of the nervous system with platinum electrodes, IEEE Transactions on Biomedical Engineering (1) (1977) 59-63.
[59] A. Merz, A.J. Bard, A stable surface modified platinum electrode prepared by coating with electroactive polymer, Journal of the American Chemical Society 100(10) (1978) 3222-3223.
[60] S.R. Kane, S.F. Cogan, J. Ehrlich, T.D. Plante, D.B. McCreery, P.R. Troyk, Electrical performance of penetrating microelectrodes chronically implanted in cat cortex, IEEE Transactions on Biomedical Engineering 60(8) (2013) 2153-2160.
[61] B.J. Black, A. Kanneganti, A. Joshi-Imre, R. Rihani, B. Chakraborty, J. Abbott, J.J. Pancrazio, S.F. Cogan, Chronic recording and electrochemical performance of Utah microelectrode arrays implanted in rat motor cortex, Journal of neurophysiology 120(4) (2018) 2083-2090.
[62] S.F. Cogan, Neural stimulation and recording electrodes, Annu. Rev. Biomed. Eng. 10 (2008) 275-309.
[63] L.A. Palmer, T.L. Davis, Receptive-field structure in cat striate cortex, Journal of neurophysiology 46(2) (1981) 260-276.
[64] E.D. Adrian, R. Matthews, The action of light on the eye: Part I. The discharge of impulses in the optic nerve and its relation to the electric changes in the retina, The Journal of Physiology 63(4) (1927) 378.
[65] W. Bair, J.R. Cavanaugh, M.A. Smith, J.A. Movshon, The timing of response onset and offset in macaque visual neurons, Journal of Neuroscience 22(8) (2002) 3189-3205.
[66] M.H. Histed, V. Bonin, R.C. Reid, Direct activation of sparse, distributed populations of cortical neurons by electrical microstimulation, Neuron 63(4) (2009) 508-522.
[67] H. Dana, T.-W. Chen, A. Hu, B.C. Shields, C. Guo, L.L. Looger, D.S. Kim, K. Svoboda, Thy1-GCaMP6 transgenic mice for neuronal population imaging in vivo, PloS one 9(9) (2014) e108697.
[68] C.L. Hughes, S.N. Flesher, J.M. Weiss, M. Boninger, J.L. Collinger, R.A. Gaunt, Perception of microstimulation frequency in human somatosensory cortex, ELife 10 (2021) e65128.
[69] T. Callier, N.W. Brantly, A. Caravelli, S.J. Bensmaia, The frequency of cortical microstimulation shapes artificial touch, Proceedings of the National Academy of Sciences 117(2) (2020) 1191-1200.
[70] M.E. Urdaneta, N.G. Kunigk, F. Delgado, S.I. Fried, K.J. Otto, Layer-specific parameters of intracortical microstimulation of the somatosensory cortex, Journal of Neural Engineering 18(5) (2021) 055007.

Supplementary materials

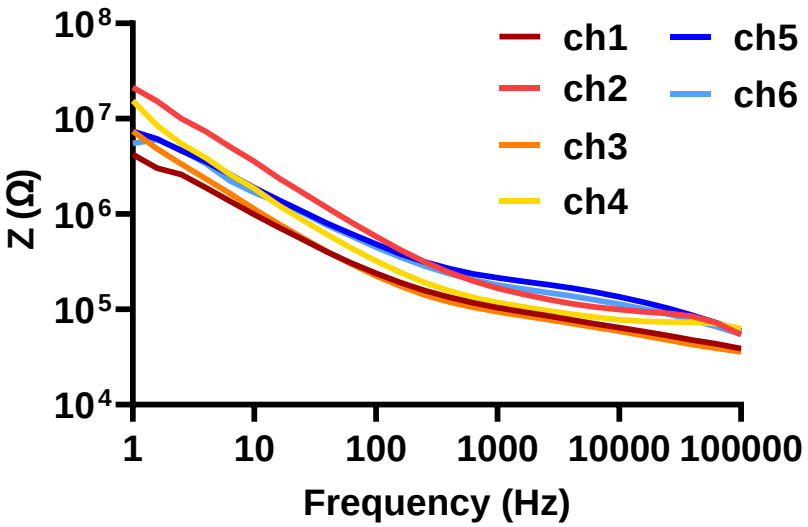

Supplementary figure 1. Impedance spectrum of the electrode sites presented in figure 8 on the day of stimulation.